PAPER

Check for updates

Chemical etching induced microporous nickel backbones decorated with metallic Fe@hydroxide nanocatalysts: an efficient and sustainable OER anode toward industrial alkaline water-splitting†

Nabeen K. Shrestha, [ID] *[a] Supriya A. Patil, [ID] [b] Jonghoon Han,[a] Sangeun Cho,[a] Akbar I. Inamdar,[a] Hyungsang Kim*[a] and Hyunsik Im [ID] *[a]

Development of cost-effective and highly efficient electrocatalysts for water splitting is crucial to produce affordable and sustainable green-hydrogen energy that can alleviate the current overreliance on fossil fuels. This work demonstrates the simple immersion-based chemical etching of nickel foam (NF) in an ethanolic $FeCl_3$ solution to generate microporous nickel (Ni) backbones decorated with hierarchically structured metallic Fe doped Ni–Fe-hydroxide nanoparticles serving as a highly promising oxygen evolution reaction (OER) electrode in alkaline water. The optimally etched NF-based OER electrode exhibits a low Tafel slope of 47.3 mV dec^{-1} and a low overpotential of 220, 270, and 310 mV at 10, 100, and 500 mA cm^{-2}, respectively. Intriguingly, this electrode also exhibits a perfectly reversible OER and HER performance between +400 and −40 mA cm^{-2} with no evidence of electrode potential decay for 80 h. Importantly, when used with an industrial-type 30 wt% KOH aqueous electrolyte and compared to a benchmark Pt/C(20wt%)‖IrO$_2$-based cell, the electrolyzer exhibits a lower cell voltage of 1.52 (*vs.* 1.56 V of Pt/C(20wt%)‖IrO$_2$-cell), 1.62 (*vs.* 1.79), 1.69 (*vs.* 1.92) and 1.79 (*vs.* 2.08) V at 10, 50, 100, and 240 mA cm^{-2}, respectively, with the cell voltage maintained for ∼100 h.

1   Introduction

Hydrogen economy is likely to be one of the most promising and competitive emission–reduction pathways for long-term global decarbonization.[1–3] Water is the most abundantly available inexhaustible and fossil-free source of hydrogen from which green hydrogen fuel can be produced *via* electrochemical water-splitting technology, provided that the electrolyzer is powered by green-electricity obtained from renewable sources. However, water electrolysis is technically hindered primarily by the sluggish oxygen evolution reaction (OER) at the anode.[4–7] In addition, noble-metal-based state-of-the-art catalysts such as Pt, RuO$_2$, or IrO$_2$ have been employed to allow water electrolysis at a lower overpotential, but these increase the costs associated with the large-scale production of hydrogen.[8]

In order to achieve sustainable water-splitting, various transition metals, metal alloys, and associated compounds have been extensively investigated as alternatives to conventional noble-metal-based catalysts.[9–20] Recently, Liu and coworkers have reported various Ni–Fe-based electrocatalysts, such as NiFe LDH/MoS$_2$, NiFeP/MXen, N-CNTs@NiS$_2$/Fe$_7$S$_8$, and Ni$_{1−x}$Fe$_x$P/PO$_3$ heterostructures, that have exhibited excellent OER performance and durability.[21–24] As an alternative to 2D flat substrates, electrically conductive foam substrates, particularly nickel foam (NF), have been widely employed as 3D porous diffusion substrates to accommodate catalysts and achieve high mass and electron transportation.[25–29] An uncontrolled high catalyst loading on NF usually obtained *via* the common deposition techniques such as drop-casting, hydrothermal, and chemical bath deposition routes, however, often leads to the deposits being stacked unevenly on top of each other. As a result, despite the high catalyst loading, stack deposition not only limits the access of the electrolyte to catalytic sites but also hinders the facile release of gas bubbles, plaguing the catalytic activity enhancement.

Herein, in contrast to the commonly used direct deposition technique for the loading of catalysts and electrochemical anodization route used to produce a porous electrode, the present study is based on the simple immersion-based chemical etching of NF in an ethanolic FeCl$_3$ solution, which produces micro- and nano-pores in the NF backbones, and the *in situ* growth of a thin film of metallic Fe-doped hierarchically structured Ni–Fe-hydroxide (hereinafter referred as Fe@Ni–Fe-

[a]Division of Physics and Semiconductor Science, Dongguk University, Seoul 04620, South Korea. E-mail: nabeenkshrestha@hotmail.com; hskim@dongguk.edu; hyunsik7@dongguk.edu

[b]Department Nanotechnology & Advanced Materials Engineering, Sejong University, Seoul-05006, South Korea

† Electronic supplementary information (ESI) available. See DOI: 10.1039/d1ta10103j

hydroxide) nanoparticles with a relatively thinner than those deposited *via* traditional deposition routes. The proposed chemical etching technique enhances active sites by preventing the over-loading of the catalyst nanoparticles, strongly binds them to the substrate, and maintains the 3D hierarchical porous network morphology of the NF backbones. This enhances mass transport, facilitating the release of O_2 bubbles from the surface, and promoting the diffusion of the electrolyte to the catalytic sites. In addition, the electron transport characteristics of the anode are strengthened, thus minimizing the issues associated with severe O_2 bubble dissipation and the low utilization of catalytic active sites due to the overgrowth of the catalyst. The aggressive evolution and trapping of gas bubbles at high current densities, in fact, block the active sites, thus hindering the access of the electrolyte and limiting the available active sites. For this reason, the effective detachment of these gas bubbles is essential for an efficient reaction, particularly at high currents or potentials.[30,31]

Most importantly, in contrast to pristine NF, optimally etched NF in an ethanolic $FeCl_3$ solution for 18 h (Fe-18h/NF) exhibits remarkably higher electrocatalytic activity, particularly with regard to the OER, with a low Tafel slope of 45.2 mV dec^{-1} and a reasonably low overpotential of 220, 270, and 310 mV at 10, 100, and 500 mA cm^{-2}, respectively, in a 1 M KOH electrolyte. In addition, the long-term electrochemical durability of the electrode for water-splitting is demonstrated at a current bias of 240 mA cm^{-2} for about 100 h using both a laboratory-scale prototype aqueous electrolyte (1 M KOH) and an industrial-type 30 wt% KOH electrolyte. It is worth noting that the OER performance of the chemically etched NF is superior to that of a state-of-the-art IrO_2/NF catalyst and is competitive with Ni–Fe and other transition-metal-based electrocatalysts deposited on NF (Table S1†). The proposed immersion-based chemical etching strategy for the fabrication of a high-performance NF-based OER electrode is also highly scalable and thus shows great promise for use in commercial water-splitting applications.

2 Results and discussion

2.1 Physical and chemical characterization of the etched NF

Fig. S1† displays images of the pristine NF before and after itching for various durations of 6, 12, 18 and 24 h in 200 μmol mL^{-1} ethanolic $FeCl_3$ at 50 °C. As the etching time increased, the NF became thinner and more fragile. Etching was more pronounced on the top tip when the NF was placed vertically in the etching bath. Thus, 1 cm^{-2} of the etched NF from the bottom part was selectively employed as the active area of the electrode for electrocatalysis. Microscopic examination of the foam was conducted *via* electron microscopy. Fig. S2a† displays an SEM image of pristine NF, showing a highly porous 3D network of Ni backbones. A magnified view of the backbones (inset of Fig. S2a†) shows Ni crystals with crystal boundaries, while a highly magnified view (Fig. S2b†) shows the surface covered with very fine grains. When the NF was immersed in 200 μmol mL^{-1} of ethanolic $FeCl_3$ as an etchant at 50 °C, pitting corrosion was observed in the early stages, as illustrated by the

presence of pin-holes on the NF surface after etching for 6 h (Fe-6h/NF; Fig. S2c†). As the immersion continued, new pits emerged and grew, forming micropores on the Ni backbones (Fig. S2e, g, and i).† NF with a uniform distribution of pores of about 20 μm was observed following the immersion performed for 18 h (Fe-18h/NF; Fig. 1a and S2g†). These pores act as diffusion paths for the electrolyte to reach active sites and for the rapid dissipation of gas from the active sites, leading to a facile mass and charge transport during water electrolysis. In addition to pore formation, the immersion of the NF in the etchant led to the *in situ* growth of dense spherical nanoparticles and their uniform distribution on the Ni backbones (Fig. 1b). The observed pitting of the Ni backbones (Fig. S2c†) was due to the strong corrosive action of the $FeCl_3$ etchant, while the chemical interactions between Fe^{3+} ions from the etchant, Ni^{2+} ions generated during the etching of the NF, and the ethanol solvent with some dissolved moistures were the key driving source responsible for the *in situ* deposition of hydroxide nanoparticles. The pore size, pore density, and size of the nanoparticles were found to vary progressively with the etching time (Fig. S2†). In particular, a longer etching duration led to a higher pore density. However, prolonged etching (*e.g.*, the Fe-24h/NF sample) led to a partial collapse of the pore structure (Fig. S2i†). On the other hand, when the etching was conducted at a lower temperature or in an etchant with a lower concentration of $FeCl_3$, no pore formation was obtained. Meanwhile, the concentration of etchant could not be increased beyond 200 μmol mL^{-1} due to limitation of solubility of $FeCl_3$ (see the Experimental section). Considering the energy costs and complexity of maintaining a symmetrical electrical field around the entire 3D NF network required in anodization route for pore formation,[32,33] the simple immersion-based chemical etching strategy proposed in the present study represents a highly promising, cost-effective approach to the mass production of microporous Ni backbones from NF.

The crystal structure of the etched NF was investigated using XRD. Fig. 1c depicts the XRD patterns obtained from pristine and etched NF samples. Compared with the pristine NF, the Fe-18h/NF sample had additional peaks other than those representing the cubic phase of the Ni substrate (JCPDS 04-0850) at about $2\theta = 11.1°$, $34.5°$, and $60.7°$. The positions of these peaks corresponded to JCPDS 38-0715, indicating the formation of α-$Ni(OH)_2$.[34–36] In addition, a small broad peak was also observed at about $43.04°$, which is closely corresponded to diffraction from the (400) plane of the $Fe(OH)_3$ cubic phase (JCPDS 022-0346). To determine the chemical composition and elemental binding states of the samples, XPS analysis of the samples was conducted. Fig. S3a† displays the elemental XPS survey spectrum, revealing that the surface of the etched NF was covered with a film composed of Cl, O, Ni, and Fe. The binding states of Ni and Fe were further investigated based on their high-resolution 2p XPS spectra. In addition to the two satellite peaks, the Ni 2p spectrum (Fig. 1d) exhibited a doublet at 873.38 eV (Ni $2p_{1/2}$) and 855.81 eV (Ni $2p_{3/2}$), which was in accordance with Ni^{2+} in $Ni(OH)_2$.[37,38] On the other hand, the doublet observed in the Fe 2p spectrum (Fig. 1e) at 724.55 eV and 712.86 eV was ascribed to Fe^{3+} in $Fe(OH)_3$.[38] In addition to

8990 | *J. Mater. Chem. A*, 2022, **10**, 8989–9000

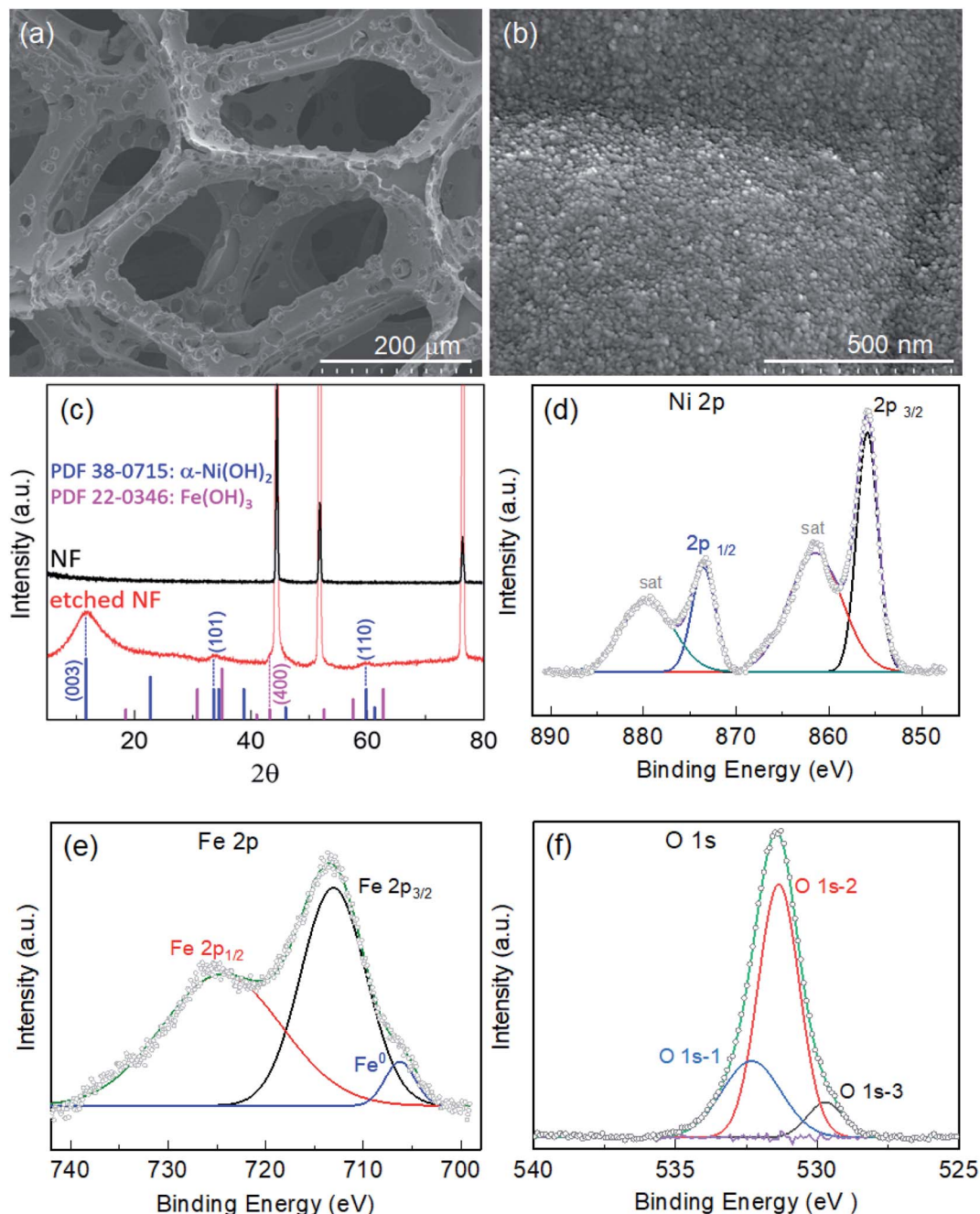This journal is © The Royal Society of Chemistry 2022

Fig. 1 SEM images of nickel foam (NF) etched for 18 h (Fe-18h/NF) in an ethanolic FeCl$_3$ solution at 50 °C: (a) surface view showing microporous Ni backbones at low magnification, and (b) a high-magnification view showing hierarchically-structured metallic Fe@Ni–Fe-hydroxide nanoparticles with a diameter of ~10 nm. (c) XRD patterns of pristine NF and NF etched for 18 h. XPS spectra of (d) Ni 2p, (e) Fe 2p, and (f) O 1s for the Fe-18h/NF sample.

the Fe^{3+} peaks, the deconvoluted Fe 2p spectrum also revealed a small metallic Fe^0 peak at about 706.34 eV. The *in situ* growth of hydroxides on the etched NF was confirmed by the O 1s spectrum (Fig. 1f), which was deconvoluted into three binding peaks at 532.3, 531.3, and 529.72 eV. The first peak at the highest binding energy (O 1s-1) corresponded to surface-absorbed water molecules, while the middle peak (O 1s-2) corresponded to lattice M–OH (M = Ni, Fe) chemisorbed hydroxyl species, and the third peak (O 1s-3) at the lowest binding energy

corresponded to oxygen atoms bound to metals.[38,39] Here, the high O 1s-2 binding energy signal at 531.3 eV was found to account for 64.53% of the total O 1s area, thus it could be clearly assigned to the presence of hydroxide species.

Overall, the XRD and XPS findings suggest that the nanoparticles were composed of metallic Fe-composited nanocrystalline Ni(OH)$_2$ and Fe(OH)$_3$. Interestingly, it is worthy to be noted that, without the addition of a reducing agent to the etchant, the deposition of metallic Fe nanoparticles was

observed. Based on the standard redox potential of $E^0_{Fe^{2+}/Fe}$ (−0.44 V) and $E^0_{Fe^{3+}/Fe^{2+}}$ (+0.77 V), we estimated the standard reduction potential of the Fe^{3+} to Fe^0 redox system to be $E^0_{Fe^{3+}/Fe}$ (+0.037 V). The details are presented in Section SI-1 of the ESI.† Because the standard reduction electrode potential of Ni is $E^0_{Ni^{2+}/Ni}$ = −0.23 V and the XPS spectrum does not reveal the presence of Fe^{2+} species in the sample (Fig. 1e), it could be assumed that there was a direct reduction of Fe^{3+} to Fe^0. However, based on the redox potential of $E^0_{Fe^{3+}/Fe^{2+}}$ (+0.77 V) and $E^0_{Fe^{3+}/Fe}$ (+0.037 V), the reduction of Fe^{3+} to Fe^{2+} is more thermodynamically favorable than the reduction of Fe^{3+} to Fe^0. Hence, the direct reduction of Fe^{3+} to Fe^0 appears unlikely. Another possibility is that the –OH moiety of the alcohol has reducing properties and can act as a reducing agent. Although the mechanism for the deposition of Fe on the NF in this work is not yet clearly understood, the reduction of various Fe oxides to metallic Fe by ethanol at high temperatures has been reported previously.[40] The introduction of the metallic Fe phase can contribute to an increase in the electrical conductivity of the *in situ* grown hydroxide film, thus facilitating electron and charge transport across the catalytic site/NF electrode and the catalytic site/electrolyte interfaces, respectively.

To acquire additional structural information, TEM analysis of the samples was conducted. In line with the SEM results shown in Fig. 1b, a TEM image of the Fe-18h/NF sample also revealed that the hydroxide film grown on the NF was composed of nearly spherical nanoparticles with a diameter of approximately 10 nm (Fig. 2a). HR-TEM images of these nanoparticles (Fig. 2b) revealed a lattice spacing of about 2.67 Å, 1.54 Å, and 1.51 Å corresponding to the (101), (110), and (113) planes, respectively, of α-Ni(OH)$_2$. Similarly, a lattice spacing of about 2.10 Å corresponding to the (400) planes of the cubic Fe(OH)$_3$ phase was also detected. This observation was also supported by the small broad XRD peak located at a 2θ of 43.04° (Fig. 1c) corresponding to the (400) plane of Fe(OH)$_3$. In addition, the XPS Fe 2p spectrum (Fig. 1e) and O 1s spectrum (Fig. 1f), particularly the O 1s-2 peak corresponding to chemisorbed hydroxyl species (M–OH, where M = Ni, Fe), also indicated the presence of Fe(OH)$_3$. However, Fe^0 phase was also not resolved in the HR-TEM image, possibly due to the amorphous state. These findings were also supported by the diffused SAED ring and dot patterns observed in Fig. 2c, indicating the coexistence of polycrystalline and amorphous phases on the etched NF surface. The amorphous phases or those with a low degree of crystallinity suggest the presence of defects in the nanoparticles, leading to a higher surface density of unsaturated sites that act as active catalytic centers, thus having a significant impact on the catalytic performance in favor of water-splitting.[41,42] It is worth noting that one such lattice defect (localized amorphization) was detected on the (110) plane, as shown in the HR-TEM image in Fig. 2b.

Furthermore, high-angle annular dark-field (HAADF) images obtained from STEM clearly displayed the uniform distribution of Ni, Fe, and O (Fig. 2d). Despite thoroughly cleaning the etched NF substrates, in accordance with the XPS survey result, the presence of Cl was also observed in the HAADF-STEM images. While examining the Cl 2p XPS spectrum of the Fe-18h/NF sample, a Cl $2p_{3/2}$ peak centered at 198.3 eV was observed, as shown in Fig. S3b.† This peak position is closer to that of NiCl$_2$ while that of the FeCl$_3$ from the etchant if presents should be located at about 199.7 eV.[43,44] This finding indicates that the hydroxide film was doped with Cl. A similar result of F-incorporation from the fluoride etchant and Cl-incorporation from the metal chlorides has been reported previously.[33,38]

2.2 Electrocatalytic performance

2.2.1 Morphology-based OER performance. Fig. 3 presents anodic polarization curves and corresponding Tafel slopes for the etched NF samples measured in a 1 M KOH electrolyte. The formation of micropores during the chemical etching process and the *in situ* growth of a spherical nanoparticle catalyst on Ni backbones were clearly observed in SEM images (ESI Fig. S2†). The particle loading and pore density, which are the key factors that decisively regulate over the concentration of active sites, and transport characteristics of mass and electron of the electrode, are directly controlled by the etching time. As such, a highly porous electrode with an optimal catalyst loading distributed uniformly over the entire electrode surface is ideal for enhancing the active site density and facilitating the transportation of high mass and electron.

To access the electrocatalytic activity on OER at a low current density, polarization was conducted at a slow scan rate of 1 mV s^{-1}. The slow scan rate was essential particularly to suppress the oxidation peak observed at about 1.4 V *vs.* RHE, as shown in Fig. S4† and accessing the OER overpotential at a low current density of 10 mA cm^{-2}. This oxidation peak is attributed to the electrochemical oxidation of (Fe–Ni)–OH phase to the catalytically favorable OER active (Fe/Ni)–OOH phase. It is worth noting that two distinct potential bias regimes were identified in the LSV curves (Fig. 3a). In the lower bias regime below 100 mA cm^{-2} (Fig. 3b), the OER was kinetically controlled, with each electrode exhibiting a similar Tafel slope (Fig. 3c). The OER performance in this regime is governed by the physical, chemical, and electronic properties of the catalytic sites and their interaction with the current collector. In particular, compared with Fe-24h/NF, the Fe-18h/NF electrode exhibited a lower overpotential, indicating a better OER performance for the electrode (Fig. 3d). In contrast, the polarization curves for the Fe-18h/NF electrode in the higher bias regime exhibited a significant increase in OER activity, outperforming the Fe-24h-/NF electrode. The enhanced OER activity of the Fe-18h/NF electrode in this regime can be attributed to high mass and electron transport, which facilitated the detachment of O$_2$ bubbles and the diffusion of the electrolyte towards the catalytic sites. These mass and electron transport characteristics of the Fe-18h/NF electrode are likely to be the result of its well-defined porous structure and uniform distribution of catalyst particles. In contrast, the excess corrosion of the NF leading to the partial collapse of the pore structure and the over-growth of nanoparticles (ESI Fig. S2i†) is likely to be the key factor that hindered mass and electron transport indisputably in the Fe-24h/NF electrode, thus decreasing its OER activity. As evidence to support the enhanced mass transfer of the Fe-18h/
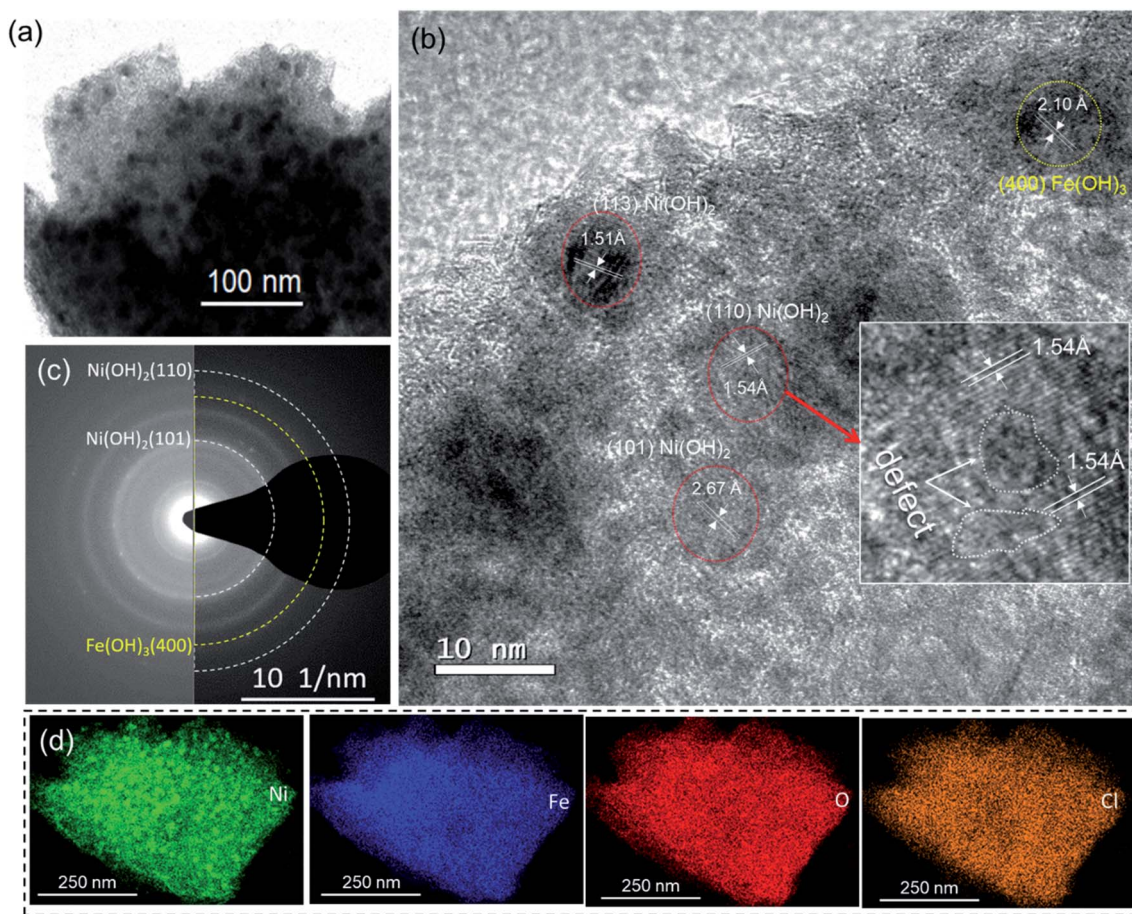
8992 | *J. Mater. Chem. A*, 2022, **10**, 8989–9000

This journal is © The Royal Society of Chemistry 2022

Fig. 2 TEM analysis of a Fe-18h/NF electrode: (a) TEM image showing ∼10 nm diameter particles, and (b) HR-TEM image showing the *d*-spacings with lattice defects on the (110) plane in the inset image. (c) SAED image showing diffused rings and dot patterns, indicating the coexistence of polycrystalline and amorphous phases. (d) HAADF mapping images showing the uniform distribution of the constituent elements.

NF electrode, chronopotentiometric curves for the closely competing Fe-18h/NF- and Fe-24h/NF-based OER electrodes were obtained and the impact of the gas bubble build-up on the surface of the electrode was evaluated at a current density of 350 mA cm^{-2}. Fig. S5† presents the large fluctuation in the OER potential for the Fe-24h/NF electrode, which was caused by the slower growth and release of the O$_2$ bubbles. This clearly indicates that the detachment of the O$_2$ bubbles from the Fe-18h/NF electrode was much easier than that from the Fe-24h/NF electrode, highlighting the enhanced mass transfer of the Fe-18h/NF electrode. Regarding the Fe-12h/NF and the Fe-6h/NF electrodes, they had a similar overpotential and Tafel slope in the kinetically controlled OER regime, while the Fe-12h/NF electrode exhibited greater OER performance in the higher bias regime.

The significant enhancement of the OER activity of the etched NF depending on the pore density and uniformity of the catalyst loading in the high potential bias regime was apparent at an overpotential (η) of 290, 320, and 330 mV (Fig. 3a and d), with the Fe-18h/NF electrode, which had the highest pore density and a uniform catalyst loading (ESI Fig. S2†), exhibiting the highest OER current density of 692.09 mA cm^{-2}. This is because higher pore density and ordered structure shortens the

dwell time of gas-bubbles in the internal space of catalyst layer. Moreover, the larger 20 μm pores on the 3D-network Ni-backbones could facilitate for the rapid dissipation of the bubbles, thereby overcoming the problem of severe coalescence of bubbles often encountered in the case of smaller sized pores.[26] In contrast to the Fe-18h/NF electrode, the NF electrodes etched for 6, 12, and 24 h had lesser number of pore density and lesser amount of catalyst particle loading for the first two samples while the agglomerated catalyst particles were obtained for the NF electrodes etched for 24 h. In addition, these samples also showed smaller electrochemically active surface area (ECSA) in Fig. S6,† indicating the lesser concentration of catalytically active sites.[45] Consequently, a significantly lower OER current density at the same η of 330 mV (337.08, 396.27, and 521.33 mA cm^{-2}, respectively) was exhibited by these 3 samples. Thus, based on the pore-density (Fig. S2†) and ECSA (Fig. S6†), the NF electrodes etched for 6, 12, 18, and 24 h exhibited the OER performance in the following order: Fe-18h/NF > Fe-24h/NF > Fe-12h/NF > Fe-6h/NF (Fig. 3).

The geometrical area-based current density (Fig. 3) is related to the ECSA of the electrodes. Hence, to investigate the influence of electrode morphology on the intrinsic catalytic activity, we attempted to eliminate the influence of the ECSA by
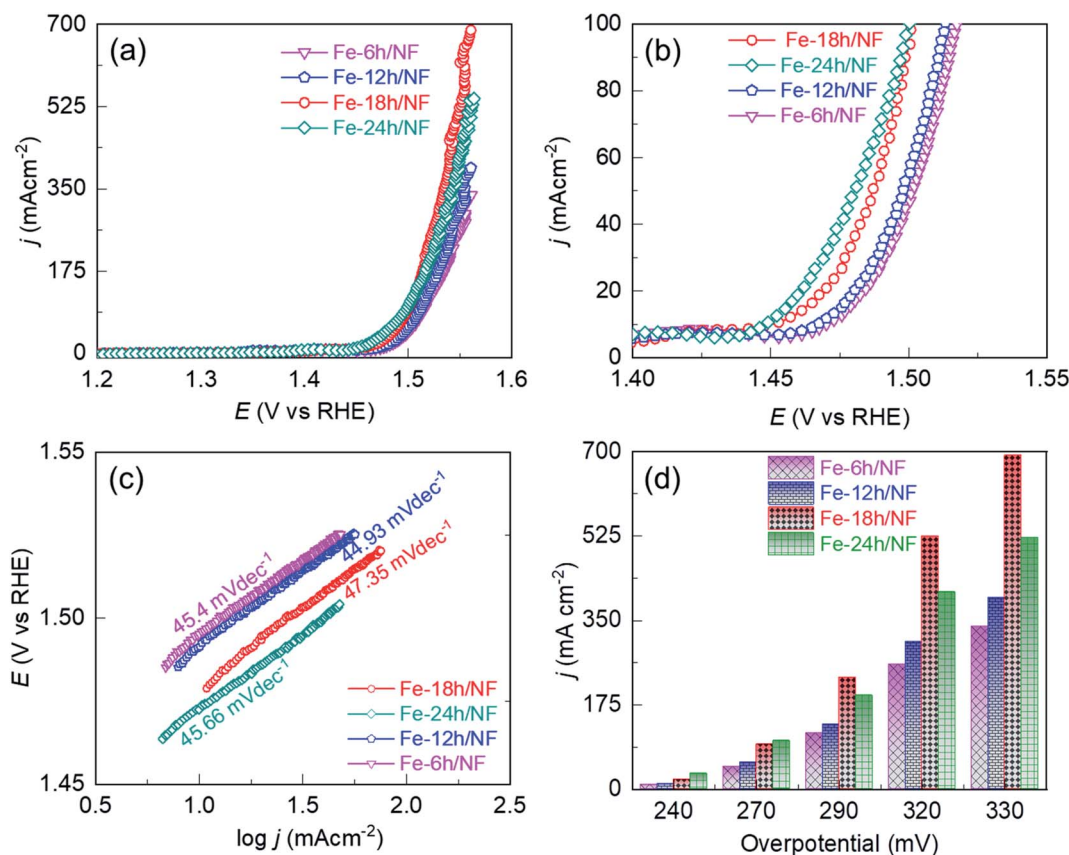
This journal is © The Royal Society of Chemistry 2022

J. Mater. Chem. A, 2022, **10**, 8989–9000 | **8993**

Fig. 3 Comparison of the electrocatalytic performance of the etched NF in a 1 M KOH solution: *iR* compensated anodic linear sweep voltammograms (LSVs) of the (a) NFs etched for 6, 12, 18, and or 24 h, (b) magnified view of (a) below 100 mA cm^{-2}, (c) corresponding Tafel slopes extracted from the LSVs, and (d) current density profiles with respect to the OER overpotential.

normalizing the geometrical-area-based current density to the ECSA of each sample. To achieve this, the double-layer capacitance (C_{dl}) was first determined from a cyclic voltammogram cascade measured in a non-faradaic potential window (Fig. S6a–e†). The ECSA was then determined according to ECSA = C_{dl}/C_s, where C_s is the specific capacitance of the electrode (Fig. S6g†).[45] The resulting ECSA-independent current density (j_{ECSA}) at a given overpotential is presented in Fig. S6f and S7.† Based on j_{ECSA}, it is evident that the electrode with the most uniform pore and catalyst nanoparticle distribution on the Ni backbones had the highest catalytic activity, and *vice versa*.

2.2.2 OER and HER performance: etched NF *vs.* state-of-the-art-catalysts. The OER and HER activities of pristine NF, etched NF, and benchmark NF electrodes loaded with an IrO$_2$ or Pt(20wt%-C) catalyst were compared volumetrically in a 1 M KOH aqueous electrolyte. Fig. 4a presents the anodic LSV curves for the electrode samples. The pristine NF exhibited the lowest OER activity with a high η of 400 and 480 mV, delivering a current density of 10 and 50 mA cm^{-2}. In contrast, the NFs produced after etching for 18 h (Fe-18h/NF) and 24 h (Fe-24h/NF) in an ethanolic FeCl$_3$ solution achieved a significantly higher OER performance. As discussed earlier, compared with Fe-18h/NF, the Fe-24h/NF electrode had a slightly better OER performance, particularly in the low current density regime below 100 mA cm^{-2}, with an η of 215 (*vs.* 220), 245 (*vs.* 247), and

270 (*vs.* 270) mV for current densities of 10, 50, and 100 mA cm^{-2}, respectively. However, the NF etched for 18 h, exhibited a better OER performance particularly at high current densities above 100 mA cm^{-2}, with an η of 290 (*vs.* 300 of the Fe-24h/NF), 300 (*vs.* 310), and 310 (*vs.* 330) mV, producing a current density of 250, 375, and 500 mA cm^{-2}, respectively (Fig. 4b).

The OER performance of the Fe-18h/NF electrode was also remarkably superior to that of a state-of-the-art IrO$_2$/NF reference electrode, which had a higher η value of 260, 310, 330, 380, and 390 mV for OER current densities of 10, 50, 100, 250, and 375 mA cm^{-2}, respectively. The OER performance of the Fe-18h/NF electrode was also highly competitive with those reported for benchmarked Ni-, Fe-, and Ni–Fe-based OER electrocatalysts (details are provided in ESI Table S1†). Most importantly, in contrast to the stringent electrochemical anodization process for obtaining porous Ni-backbone on NFs,[32,33] the simple chemical etching process in the present study not only produced a uniform distribution of micropores on the Ni backbones, but led to an outstanding OER performance, achieving a current density of 500 mA cm^{-2} at η = 310 mV, thus out-performing electrochemically etched NF-based electrodes. In particular, electrochemically etched NF electrodes reported an OER current density of 500 mA cm^{-2} at higher η of 334 (ref. 32) and 350 mV.[33] The OER performance of the Fe-18h/NF electrode was also even better than that of a porous Ni

8994 | *J. Mater. Chem. A*, 2022, **10**, 8989–9000

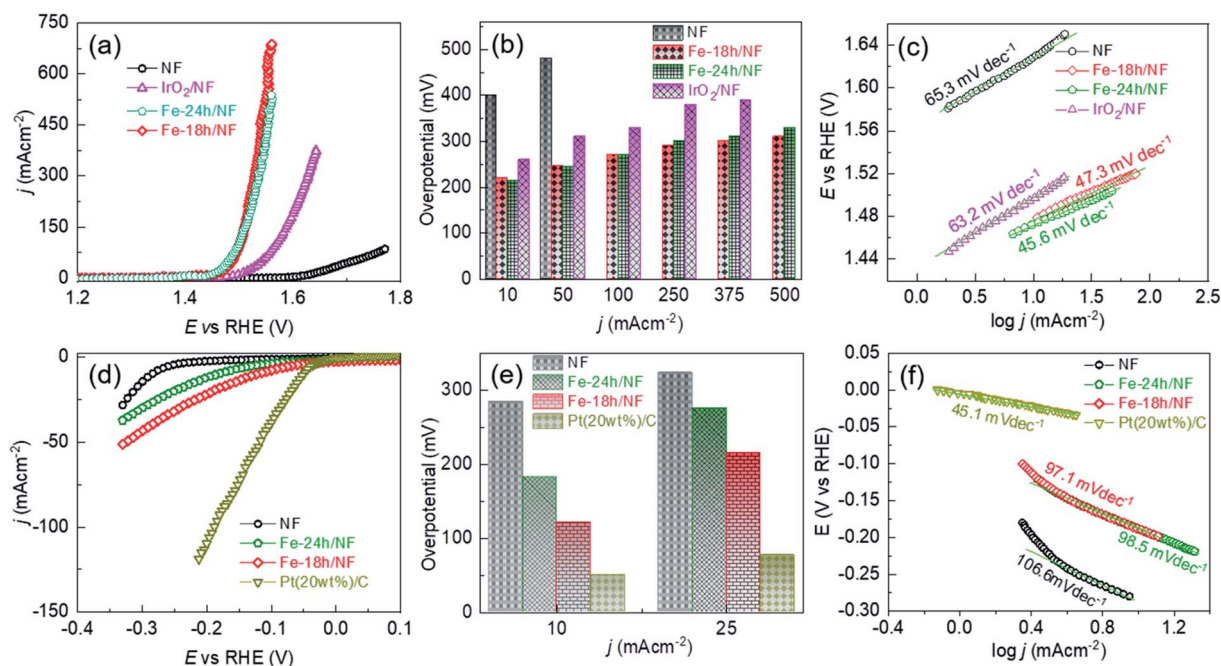This journal is © The Royal Society of Chemistry 2022

Fig. 4 Comparison of the electrocatalytic performance of the etched NFs and a benchmark catalyst in a 1 M KOH solution: (a) *iR* compensated anodic LSVs for the pristine NF, etched NF, and benchmark IrO$_2$/NF electrodes, (b) overpotential profiles with respect to the OER current density, and (c) corresponding Tafel slopes extracted from the LSVs. (d) *iR* compensated cathodic LSVs of the pristine NF, etched NFs, and benchmark Pt(20wt%)-C/NF electrodes, (e) overpotential profiles with respect to the HER current density, and (f) corresponding Tafel slopes extracted from the LSVs.

electrode (10 mA cm^{-2} @ η = 300 mV) obtained *via* phase inversion,[46] and a spiky Ni electrode (100 mA cm^{-2} @ η = 300 mV in a 25 wt% KOH electrolyte) obtained *via* femtosecond laser structuring.[47] The obtained superior OER performance of the etched NF electrode of this work over the already reported nanostructured Ni electrodes can be attributed to the synergistic interplay among the uniformly distributed metallic Fe@Ni–Fe-hydroxide nanocrystals, lattice defects and gas/electrolyte diffusible microporous Ni-backbones.

ESI Fig. S8† shows that the Fe-18h/NF electrode had the highest ECSA (719.09 cm^{-2}) followed by Fe-24h/NF (695.90 cm^{-2}), IrO$_2$/NF (402.27 cm^{-2}), and pristine NF (387.73 cm^{-2}). Thus, in addition to having a uniform distribution of micropores and catalyst nanoparticles on the Ni backbones, the superior OER performance of the etched NF electrodes can also be attributed to the abundantly available electrochemical active sites. ESI Fig. S9† presents Nyquist plots and corresponding fitted parameters extracted from electrochemical impedance spectra measured at a bias of 1.5 V *vs.* RHE in a 1 M KOH electrolyte. The Fe-18h/NF and the Fe-24h/NF electrodes exhibited a significantly lower charge transfer resistance than did the IrO$_2$/NF and pristine NF electrodes, leading to the faster charge transfer between the electrochemically active catalytic sites and the electrolyte during the OER. The accelerated faradaic response and the consequently superior OER kinetics for the etched NF electrodes can be attributed to the synergic effect between the metallic Fe and the hydroxides in establishing a good electrical contact across the interface between the parent hydroxides ((Fe/Ni)–OH) and the corresponding oxyhydroxides

((Fe/Ni)–OOH) formed during the application of the anodic bias, thus decreasing the Schottky barriers.[48–50]

To provide further insight into the electrode kinetics during the OER process, the Tafel slopes derived from the corresponding anodic polarization curves (Fig. 4a) were estimated. As shown in Fig. 4c, both etched NF electrodes exhibited similar Tafel slopes (47.3 and 45.6 mV dec^{-1}). However, these slopes were much lower than those of the pristine NF (65.3 mV dec^{-1}) and the IrO$_2$/NF (63.2 mV dec^{-1}) electrodes. These exceptionally low Tafel slopes are probably due to the coexistence of metallic Fe atoms and Ni–Fe-hydroxide nanocrystalline-clusters, which promotes faster and highly efficient OER kinetics. The HER performance of the electrodes was also assessed, as shown in Fig. 4d–f. The state-of-the-art Pt(20wt%)-C/NF-based HER electrode produced the best performance with a low HER overpotential and a low Tafel slope. Nevertheless, the Fe-18h/NF electrode also exhibited a significantly enhanced HER performance in comparison to the Fe-24h/NF and pristine NF electrodes, with a lower HER overpotential and Tafel slope.

2.2.3 Electrochemical reversibility and durability of the Fe-18h/NF electrode. In the anodic and cathodic LSV analysis, the Fe-18h/NF electrode conspicuously exhibited a strong color contrast between dark black and light grey during the OER and HER, respectively, in a 1 M KOH aqueous electrolyte. The cyclic voltammetry of the electrode also exhibited a pair of reversible anodic and cathodic redox peaks at about 1.44 and 1.35 V *vs.* RHE (ESI Fig. S10†). These reversible redox peaks and the corresponding color-switching can be attributed to the reversible electron injection (Fe/Ni–OH + OH$^-$ ↔ Fe/Ni–OOH + H$^+$ + e$^-$)[51]

This journal is © The Royal Society of Chemistry 2022

J. Mater. Chem. A, 2022, **10**, 8989–9000 | **8995**

for an anodic and cathodic bias, respectively. On the basis of this, the electrochemical reversibility of the electrode for the OER and HER was investigated. Based on the LSV presented in Fig. 4a and d, the electrode was polarized anodically and cathodically at a current density of $+400$ and -40 mA cm^{-2}, respectively, and the resulting chronopotentiometric response is presented in Fig. 5a. Notably, there was no apparent loss in the electrode potential in either bias direction for up to 80 h of operation (Fig. 5a and ESI Fig. S10b†), indicating that the Fe-18h/NF electrode can be reversibly polarized to facilitate the HER and OER without losing efficiency. This concept on reversible polarization and electrochemical reversibility for the HER/OER are industrially advantageous when unavoidable problems arise, such as electrode corrosion and the loss of catalytic activity, which are encountered when the depolarization of the electrode leads to a reversed bias. This often happens when the catalyst is assimilated with renewable H$_2$ production *via* water electrolysis and powered by a photovoltaic device.[52,53] Overall, our proposed electrode exhibited long-term electrochemical durability for 80 h under a periodic bias of $+400$ and -40 mA cm^{-2}.

The electrochemical durability of the Fe-18h/NF electrode was investigated further under a stress bias of 10, 50, 100, 200,

and 240 mA cm^{-2} between two Fe-18h/NF electrodes working as the cathode and anode of an electrolyzer for 24 h (total 120 h) in a 1 M KOH aqueous electrolyte. The obtained chronopotentiometric traces revealed no apparent change in the cell voltage (V_{cell}) for each bias, representing a high electrochemical durability for up to 120 h (Fig. 5b). This finding was supported by the similar anodic and cathodic LSVs for the anode and cathode obtained before and after the 120 h durability test (Fig. 5c and d). The slightly higher current density for the electrolyzer after the durability test could be due to the increase in the number of active sites during the long-term *in situ* activation of the electrodes in the stability test. Note that the cell voltage (V_{cell}) is the potential difference measured between two electrodes of the electrolyzer, which has real physical meaning in practical applications. In this case, *iR* losses are usually not accounted for. Meanwhile, the working electrode potential, E (V *vs.* RHE) in a half-cell configuration was compensated for *iR* loss to precisely determine the overpotential (*i.e.*, the extra potential required by the electrode over the thermodynamic potential) for the OER and HER using the following relations: $\eta_{OER} = E_{RHE} - 1.23$ V for OER and $\eta_{HER} = E_{RHE} - 0.0$ V for HER, where E_{RHE} is the electrode potential measured in the scale of RHE, and 1.23 V
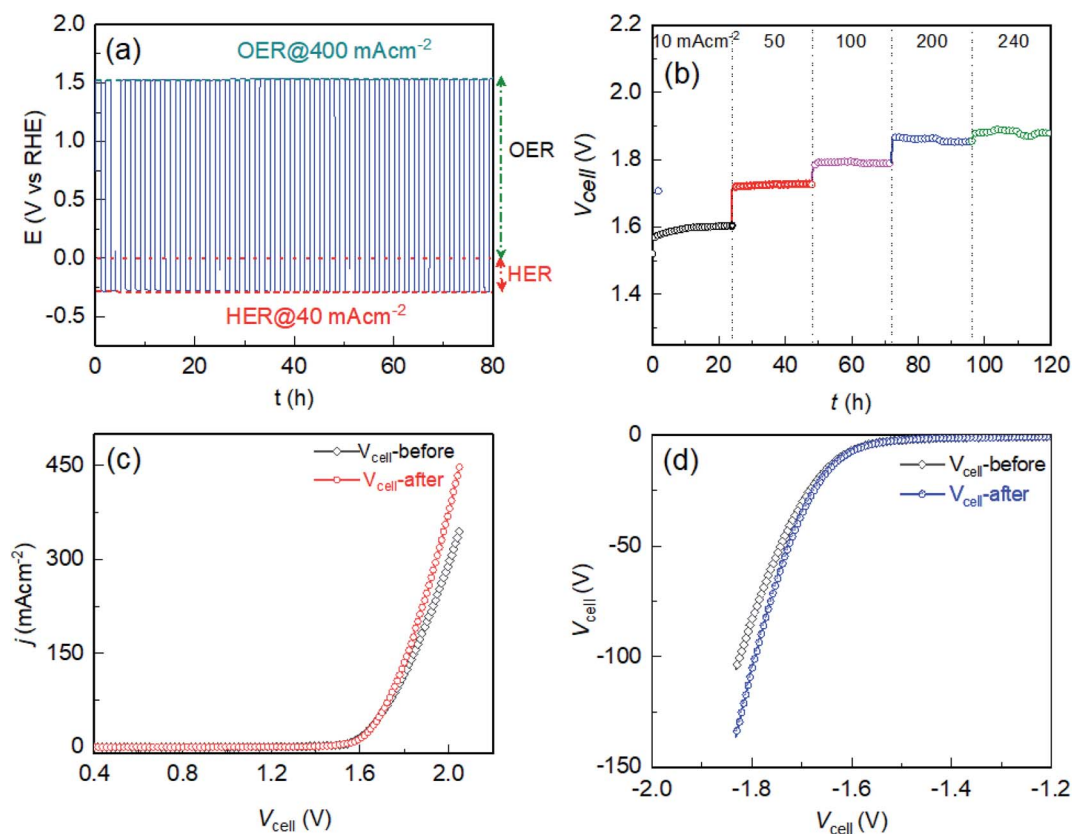

Fig. 5 Electrochemical reversibility and stability in a 1 M KOH solution: (a) chronopotentiometric response when periodically polarizing the Fe-18h/NF electrode between $+400$ and -40 mA cm^{-2} for 80 h, showing perfect electrochemical reversibility between the OER and HER. (b) Cell voltages (without *iR* compensation) between two identical Fe-18h/NF electrodes at a stress bias of 10, 50, 100, 200, or 240 mA cm^{-2} for 120 h, showing high long-term electrochemical stability. Without *iR* compensated LSVs of the cell before and after the 120 h stability test: (c) anodic LSVs for the Fe-18h/NF anode with respect to the Fe-18h/NF cathode, and (d) cathodic LSVs for the Fe-18h/NF cathode with respect to the Fe-18h/NF anode. Inset image in (d) shows the cell voltage profile with respect to the current density, extracted from the LSVs of the anode and cathode after the stability test shown in (c) and (d).

8996 | *J. Mater. Chem. A*, 2022, **10**, 8989–9000

This journal is © The Royal Society of Chemistry 2022

and 0.0 V are the thermodynamic potentials for OER and HER, respectively. Consequently, some small overpotential differences can be observed in between E (V $vs.$ RHE) and V_{cell} in Fig. 4a, d and 5c, d.

2.2.4 Electrode performance toward industrial alkaline water-splitting. To test the practical application of the Fe-18h/NF electrode toward commercial alkaline water-splitting applications, an electrolyzer consisting of a pair of Fe-18h/NF‖Fe-18h/NF electrodes was tested in a 30 wt% KOH aqueous electrolyte. Fig. 6a presents the LSVs of the anodes, revealing that the Fe-18h/NF‖Fe-18h/NF pair offered a stronger water-splitting performance than did the benchmark Pt(20wt%)-C/NF‖IrO$_2$/NF cell. Specifically, compared to the benchmark Pt(20wt%)-C/NF-based cell, the Fe-18h/NF‖Fe-18h/NF cell achieved a current density of 10, 50, 100, and 250 mA cm^{-2} at a cell voltage of 1.52 ($vs.$ 1.56), 1.62 ($vs.$ 1.79), 1.69 ($vs.$ 1.92), and 1.84 ($vs.$ 2.15) V, respectively (Fig. 6b). In addition, the faradaic efficiency of the Fe-18h/NF electrode for the HER and OER was determined by measuring the volume of H$_2$ and O$_2$ evolved using a conventional water displacement method. The current efficiency of the Fe-18h/NF electrode was found to be closer to the theoretical value, as shown in Fig. S11.† This indicates that there were no other side reactions at the cathode or anode, suggesting that the current observed in the electrolysis was solely associated with the HER and OER. Furthermore, the cell voltage was well-maintained when a stress bias equivalent to the corresponding current density was applied for 96 h (Fig. 6c). It is worth noting that the benchmark Pt(20wt%)-C/NF‖IrO$_2$/NF cell exhibited a detectable voltage decay, particularly under a bias of 240 mA cm^{-2}, indicating that the benchmark electrode pair lost electrochemical stability at higher current biases.

To provide further insight into the material durability of the electrode after long-term electrochemical stability testing for 96 h, the Fe-18h/NF anode was examined using XPS, XRD, SEM, and STEM. Compared to Fig. 1d, e, ESI Fig. S12† shows that the 2p peaks of the Ni 2p and Fe 2p XPS spectra of the electrode after the stability test shifted slightly toward a higher binding energy by 0.18 and 0.20 eV, respectively. This could be

attributed to the oxidation of the hydroxides of the electrode into the corresponding (Fe–Ni)–OOH phase. This interpretation was supported by the Raman shifts (Fig. S13†), which clearly showed a pair of peaks corresponding to the M–OOH phase (M = Ni, Fe).[54,55] In addition, the area under the Fe^0 peak decreased while that of the O 1s peaks increased, supporting the likely oxidation of M–OH into M–OOH. The XRD analysis, however, did not reveal peaks from the M–OOH phase. This could be due to the very thin film of M–OOH that formed on the surface of the hydroxide particles or due to the formation of an amorphous M–OOH phase. On the other hand, the XRD patterns indicated the presence of the initially existing prominent diffraction peaks for the (003) and (101) planes from α-Ni(OH)$_2$ even after the durability test (ESI Fig. S14a†). In addition, an additional diffraction peak corresponding to the (006) plane of α-Ni(OH)$_2$ also appeared after the durability test. This crystallographic planes could be equally active for water-splitting as demonstrated by the initially existing (003) and (101) planes of the α-Ni(OH)$_2$. As such, $in situ$ catalytic site enhancement can be realized when the electrodes are employed for long-term water electrolysis. This could be the reason for the slight improvement in the current density of the electrolyzer after the long-term durability test (Fig. 5c and d). Most importantly, the peaks after the durability test were sharper than the initial peaks (compare ESI Fig. S14a† and 1c), indicating the improved crystallization of the $in situ$ grown α-Ni(OH)$_2$ nanoparticles. This finding was also supported by an SEM surface view of the electrode, which showed an increase in the particle size from ~10 nm to ~20 nm (compare ESI Fig. S14b† and 1b). However, the initial spherical morphology of the nanoparticles remained intact without deformation. Similarly, HAADF images (ESI Fig. S15†) obtained from STEM revealed the uniform distribution of Ni, Fe, O and Cl within the electrode, as was observed before the durability test. These findings confirm the long-term electrochemical durability of the Fe-18h/NF electrode, demonstrating that it is a promising candidate as an efficient and sustainable anode material for use in industrial alkaline water-splitting applications.
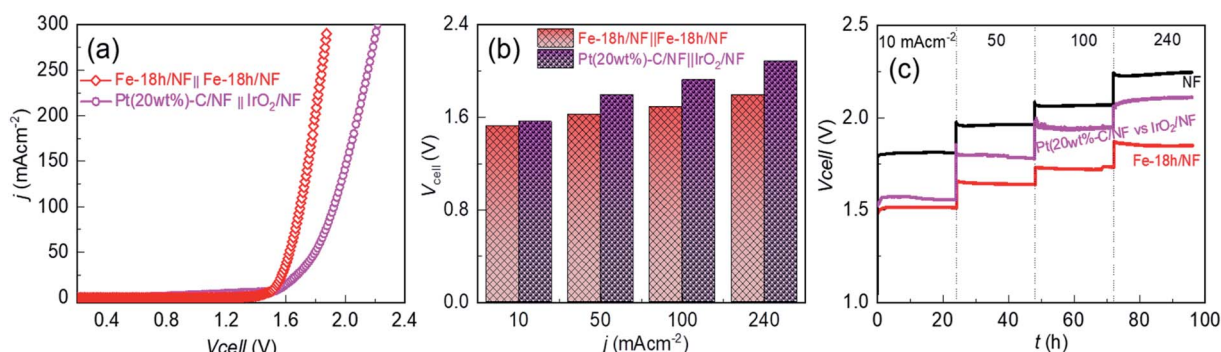

Fig. 6 Electrochemical activity and durability in an industrial-type 30 wt% KOH solution: (a) without iR compensated anodic LSV for the Fe-18h/NF anode with respect to the Fe-18h/NF cathode, and anodic LSV for the IrO$_2$/NF anode with respect to the Pt(20wt%-C)/NF cathode. (b) Cell voltage profiles with respect to the current density, extracted from the corresponding LSVs. (c) Cell voltages (without iR compensation) between two identical electrodes at a stress bias of 10, 50, 100, or 240 mA cm^{-2} for 96 h, showing the outstanding long-term electrochemical durability of the Fe-18h/NF electrode.

This journal is © The Royal Society of Chemistry 2022

J. Mater. Chem. A, 2022, **10**, 8989–9000 | **8997**

3   Conclusions

This work presents a cost-effective design for the scalable production of an efficient and sustainable alkaline OER electrode. The key interest of this work lies on the morphological engineering strategy of 3D-NF *via* chemical etching for obtaining porous electrode to enhance the number of active sites while minimizing the detrimental electron and mass transport (*i.e.*, inward diffusion of OH^- and outward diffusion of oxygen bubbles) limitations. A readily scalable approach to the fabrication of microporous Ni backbones decorated with metallic Fe composited Ni- and Fe-hydroxide nanoparticles on NF was demonstrated using the immersion-based chemical etching of NF in an ethanolic $FeCl_3$ solution at 50 °C. The pores and nanoparticles grew progressively and uniformly with an increase in the etching time. Compared to advanced non-noble metal-based water-splitting catalysts, including electrochemically etched NF and benchmark Pt(20wt%)-C/IrO_2-based HER/OER electrodes, the optimally etched NF demonstrated an outstanding catalytic performance, with a low OER overpotential and cell voltage producing a high current density and strong long-term electrochemical durability (~100 h) in both 1 M KOH and industrial-type 30 wt% KOH aqueous electrolytes. The cooperative interplay between the uniformly distributed micropores and metallic Fe doped hydroxide nanocatalysts with the localized amorphization in the crystal lattice facilitating mass and charge transportation is likely to be the key for promoting the access of the electrolyte to all available catalytic sites and leading to the release of O_2 bubbles from these sites, thus demonstrating an outstanding electrocatalytic performance for potential water-splitting applications. In addition, the chemically etched NF-electrode showed a high robustness upon power interruptions, which might be promising for intermittent energy resources powered water-electrolysis.

4   Experimental section

4.1   Reagents and materials

Iron(III) chloride ($FeCl_3$, ≥99.99%), potassium hydroxide (≥85%), hydrochloric acid (37%), hydrochloric acid (37%), ethanol (≥99.5%), and acetone (≥99.9%) were purchased from Sigma-Aldrich. Nickel foams (NF) with a thickness of 1.6 mm and a cell size of 450 μm was purchased from Alantum Corporation (South Korea). As the substrate, the NF was cut into 1×5 cm^2 pieces and washed sequentially for 10 minutes in 1 M HCl, deionized water, ethanol, and acetone with an ultrasonicator. Finally, the washed NF was dried at room temperature for 24 h.

4.2   Chemical etching of the NF

A freshly prepared ethanolic solution of $FeCl_3$ (200 μM mL^{-1}) was stored overnight for settlement of insoluble excess $FeCl_3$. The clear solution was pipetted into a 15 mL glass reagent bottle and the washed NF substrates (1×5 cm^2) were completely immersed in the solution for etching times of 6, 12, 18, or 24 h at 50 °C with the lid of the reagent bottles closed. After the completion of etching, the immersed NF was washed thoroughly with ethanol. Finally, the sample was dried under a stream of N_2 gas.

4.3   Characterization of the etched NF

The morphology of the etched NF samples was investigated using a field-emission scanning electron microscope (FE-SEM, Hitachi S-4800) and a scanning transmission electron microscope (STEM, Talos™ F200X). The elemental composition was determined using an energy dispersive X-ray (EDX) spectrometer (Oxford 6587). The distribution of the elements was analyzed by generating elemental maps using the STEM. X-ray photoelectron spectroscopy (XPS) was conducted to determine the binding states of the elements present in the samples using an ESCALAB 250Xi spectrometer (ThermoFisher) and monochromatized Al Kα X-rays for excitation. X-ray diffraction (XRD) analysis was conducted using an X'Pert diffractometer (Malvern PANalytical) equipped with a Cu Kα radiation source (λ = 0.15418 nm) in a range from (2θ) 5° to 60° with a scanning step size of 0.01°.

4.4   Electrochemical measurements

Electrochemical experiments were performed in a three-electrode system configured with an NF-based electrode that served as the working electrode. A graphite rod and a saturated calomel electrode (SCE) served as the counter and reference electrodes, respectively. All voltammetry experiments were conducted using a VersaSTA-3 electrochemical workstation (Princeton Applied Research), and the recorded potential was converted to the reversible hydrogen electrode (RHE) scale according to eqn (1).

$$E_{RHE} = E_{SCE} + E_{SCE}^{\circ} + (0.059) \times pH \qquad (1)$$

where E_{SCE}° is the standard potential of an SCE electrode (0.244 V), and pH is the measured pH of the aqueous 1 M KOH electrolyte solution. Prior to measurement, the electrodes were electrochemically activated *via* cyclic voltammetry at a scan rate of 100 mV s^{-1} until stable voltammograms were obtained. To evaluate the OER and HER overpotential, linear sweep voltammograms (LSVs) were produced at a scan rate of 1 mV s^{-1}. Electrochemical impedance spectroscopy (EIS) was conducted using the VersaSTA-3 electrochemical workstation. Unless otherwise stated, all LSVs were reported with *iR* drop compensation. The electrochemical stability of the electrode was measured chronopotentiometrically using a BioLogic Science Instruments electrochemical workstation, which can measure a maximum current of 240 mA.

Author contributions

Nabeen K. Shrestha: conceptualization, investigation, experimental analysis, methodology, and writing original draft. Supriya A. Patil: methodology, experimental analysis, data curation, and writing. Jonghoon Han: methodology, and experimental analysis. Sangeun Cho: methodology, and writing & editing. Akbar I. Inamdar: experimental analysis, writing and

8998 | *J. Mater. Chem. A*, 2022, **10**, 8989–9000

This journal is © The Royal Society of Chemistry 2022

revisions. Hyungsang Kim: conceptualization, and funding. Hyunsik Im: conceptualization, funding, and review & editing.

Conflicts of interest

The authors declare that there is no conflict of interest.

Acknowledgements

References

1 I. Staffell, D. Scamman, A. Velazquez Abad, P. Balcombe, P. E. Dodds, P. Ekins, N. Shah and K. R. Ward, *Energy Environ. Sci.*, 2019, **12**, 463.

2 E. S. Hanley, J. P. Deane and B. P. Ó. Gallachóir, *Renewable Sustainable Energy Rev.*, 2018, **82**, 3027.

3 M. Noussan, P. P. Raimondi, R. Scita and M. Hafner, *Sustainability*, 2021, **13**, 298.

4 Z. W. She, J. Kibsgaard, C. F. Dickens, I. Chorkendorff, J. K. Nørskov and T. F. Jaramillo, *Science*, 2017, **355**, 146.

5 B. You and Y. Sun, *Acc. Chem. Res.*, 2018, **51**, 1571.

6 X. Zou and Y. Zhang, *Chem. Soc. Rev.*, 2015, **44**, 5148.

7 L. Gao, C. Tang, J. Liu, L. He, H. Wang, Z. Ke, W. Li, C. Jiang, D. He, L. Cheng and X. Xiao, *Energy & Environmental Materials*, 2021, **4**, 392.

8 Y. Jiao, Y. Zheng, M. Jaroniec and S. Z. Qiao, *Chem. Soc. Rev.*, 2015, **44**, 2060.

9 F. Lyu, Q. Wang, S. M. Choi and Y. Yin, *Small*, 2019, **15**, 1804201.

10 Y. Chen, K. Rui, J. Zhu, S. X. Dou and W. Sun, *Chem.–Eur. J.*, 2019, **25**, 703.

11 A. T. A. Ahmed, S. M. Pawar, A. I. Inamdar, H. Im and H. Kim, *Int. J. Energy Res.*, 2020, **44**, 1798.

12 D. V. Shinde, S. A. Patil, K. Cho, D. Y. Ahn, N. K. Shrestha, R. S. Mane, J. K. Lee and S. H. Han, *Adv. Funct. Mater.*, 2015, **25**, 5739.

13 H. T. Bui, D. Y. Ahn, N. K. Shrestha, M. M. Sung, J. K. Lee and S. H. Han, *J. Mater. Chem. A*, 2016, **4**, 9781.

14 S. A. Patil, S. Cho, Y. Jo, N. K. Shrestha, H. Kim and H. Im, *Chem. Eng. J.*, 2021, **426**, 130773.

15 D. S. Raja, C.-L. Huang, Y.-A. Chen, Y. Choi and S.-Y. Lu, *Appl. Catal., B*, 2020, **279**, 119375.

16 N. K. Shrestha, S. A. Patil, S. Cho, Y. Jo, H. Kim and H. Im, *J. Mater. Chem. A*, 2020, **8**, 24408.

17 A. I. Inamdar, H. S. Chavan, B. Hou, C. H. Lee, S. U. Lee, S. N. Cha, H. Kim and H. Im, *Small*, 2020, **16**, 1905884.

18 F. Dionigi, Z. Zeng, I. Sinev, T. Merzdorf, S. Deshpande, M. B. Lopez, S. Kunze, I. Zegkinoglou, H. Sarodnik, D. Fan, A. Bergmann, J. Drnec, J. F. de Araujo, M. Gliech, D. Teschner, J. Zhu, W. X. Li, J. Greeley, B. R. Cuenya and P. Strasser, *Nat. Commun.*, 2020, **11**, 2522.

19 A. I. Inamdar, H. S. Chavan, S. M. Pawar, H. Kim and H. Im, *Int. J. Energy Res.*, 2020, **44**, 1789.

20 N. Yu, W. Cao, M. Huttula, Y. Kayser, P. Hoenicke, B. Beckhof, F. Lai, R. Dong, H. Sun and B. Geng, *Appl. Catal., B*, 2020, **261**, 118193.

21 X.-P. Li, L.-R. Zheng, S.-J. Liu, T. Ouyang, S. Ye and Z.-Q. Liu, *Chin. Chem. Lett.*, 2022, DOI: 10.1016/j.cclet.2021.12.095.

22 J. Chen, Q. Long, K. Xiao, T. Ouyang, N. Li, S. Ye and Z.-Q. Liu, *Sci. Bull.*, 2021, **66**, 1063.

23 J.-Y. Wang, W.-T. Liu, X.-P. Li, T. Ouyang and Z.-Q. Liu, *Chem. Commun.*, 2020, **56**, 1489.

24 C. Huang, Y. Zou, Y.-Q. Ye, T. Ouyang, K. Xiao and Z.-Q. Liu, *Chem. Commun.*, 2019, **55**, 7687.

25 J. Luo, J. H. Im, M. T. Mayer, M. Schreier, M. K. Nazeeruddin, N. G. Park, S. D. Tilley, H. J. Fan and M. Grätzel, *Science*, 2014, **345**, 1593.

26 Y. J. Kim, A. Lim, J. M. Kim, D. Lim, K. H. Chae, E. N. Cho, H. J. Han, K. U. Jeon, M. Kim, G. H. Lee, G. R. Lee, H. S. Ahn, H. S. Park, H. Kim, J. Y. Kim and Y. S. Jung, *Nat. Commun.*, 2020, **11**, 4921.

27 Y. Jo, S. Cho, J. Seo, A. T. A. Ahmed, C. H. Lee, J. H. Seok, B. Hou, S. A. Patil, Y. Park, N. K. Shrestha, S. U. Lee, H. Kim and H. Im, *ACS Appl. Mater. Interfaces*, 2021, **13**, 53725.

28 A. T. A. Ahmed, A. S. Ansari, S. M. Pawar, B. Shong, H. Kim and H. Im, *Appl. Surf. Sci.*, 2021, **539**, 148229.

29 T. Kou, S. Wang, R. Shi, T. Zhang, S. Chiovoloni, J. Q. Lu, W. Chen, M. A. Worsley, B. C. Wood, S. E. Baker, E. B. Duoss, R. Wu, C. Zhu and Y. Li, *Adv. Energy Mater.*, 2020, **10**, 2002955.

30 Z. Zhang, B. He, L. Chen, H. Wang, R. Wang, L. Zhao and Y. Gong, *ACS Appl. Mater. Interfaces*, 2018, **10**, 38032.

31 Y. Zhou, Y. Yang, X. Zhu, D. Ding Ye, R. Chen and Q. Liao, *J. Power Sources*, 2021, **507**, 230260.

32 X. F. Chuah, C. T. Hsieh, C. L. Huang, D. Senthil Raja, H. W. Lin and S. Y. Lu, *ACS Appl. Energy Mater.*, 2019, **2**, 743.

33 Y. J. Son, K. Kawashima, B. R. Wygant, C. H. Lam, J. N. Burrow, H. Celio, A. Dolocan, J. G. Ekerdt and C. B. Mullinsn, *ACS Nano*, 2021, **15**, 3468.

34 J. Yu, S. Pan, Y. Zhang, Q. Liu and B. Li, *Front. Mater.*, 2019, **6**, 124.

35 M. Aghazadeh, M. Ghaemi, B. Sabour and S. Dalvand, *J. Solid State Electrochem.*, 2014, **18**, 1569.

36 D. S. Hall, D. J. Lockwood, C. Bock and B. R. MacDougall, *Proc. R. Soc. A*, 2015, **471**, 20140792.

37 X. Chen, C. Long, C. Lin, T. Wei, J. Yan, L. Jiang and Z. Fan, *Electrochim. Acta*, 2014, **137**, 352.

38 Y. Wei, C. H. Shin, E. B. Tetteh, B. J. Lee and J. S. Yu, *ACS Appl. Energy Mater.*, 2020, **3**, 822.

39 Y. J. Ye, N. Zhang and X. X. Liu, *J. Mater. Chem. A*, 2017, **5**, 24208.

40 M. G. Rosmaninho, F. C. C. Moura, L. R. Souza, R. K. Nogueira, G. M. Gomes, J. S. Nascimento, M. C. Pereira, J. D. Fabris, J. D. Ardisson, M. S. Nazzarro, K. Sapag, M. H. Araújo and R. M. Lago, *Appl. Catal., B*, 2012, **115–116**, 45.

41 S. Anantharaj and S. Noda, *Small*, 2020, **16**, 1905779.

This journal is © The Royal Society of Chemistry 2022

J. Mater. Chem. A, 2022, **10**, 8989–9000 | **8999**

42 D. Zhang, J. Z. Soo, H. H. Tan, C. Jagadish, K. Catchpole and S. K. Karuturi, *Adv. Energy Mater.*, 2020, **2**, 2000071.

43 L. Liu, F. Tian, X. Wang, Z. Yang and X. Wang, *Ionics*, 2013, **19**, 9.

44 A. P. Grosvenor, B. A. Kobe, M. C. Biesinger and N. S. McIntyre, *Surf. Interface Anal.*, 2004, **36**, 1564.

45 C. C. L. McCrory, S. Jung, J. C. Peters and T. F. Jaramillo, *J. Am. Chem. Soc.*, 2013, **135**, 16977.

46 R. Ding, S. Cui, J. Lin, Z. Sun, P. Du and C. Chen, *Catal. Sci. Technol.*, 2017, **7**, 3056.

47 F. Rieck Genannt Best, J. Koch, G. Lilienkamp, F. Körkemeyer, H. J. Maier, J. Caro and K. Lange, *Int. J. Electrochem.*, 2018, **12**, 1–12.

48 H. Xu, Z. X. Shi, Y. X. Tong and G. R. Li, *Adv. Mater.*, 2018, **30**, 1705442.

49 A. Aijaz, J. Masa, C. Rösler, W. Xia, P. Weide, A. J. R. Botz, R. A. Fischer, W. Schuhmann and M. Muhler, *Angew. Chem., Int. Ed.*, 2016, **55**, 4087.

50 S. Niu, Y. Sun, G. Sun, D. Rakov, Y. Li, Y. Ma, J. Chu and P. Xu, *ACS Appl. Energy Mater.*, 2019, **2**, 3927.

51 N. K. Shrestha, M. Yang and P. Schmuki, *Electrochem. Solid-State Lett.*, 2010, **13**, 6.

52 J. Divisek, J. Mergel and H. Schmitz, *Int. J. Hydrogen Energy*, 1990, **15**, 105.

53 B. C. M. Martindale and E. Reisner, *Adv. Energy Mater.*, 2016, **6**, 1502095.

54 L. Bai, S. Lee and X. Hu, *Angew. Chem.*, 2021, **60**, 3095.

55 H. S. Chavan, C. H. Lee, A. I. Inamdar, J. Han, S. Park, S. Cho, N. K. Shrestha, S. U. Lee, B. Hou, H. Im and H. Kim, *ACS Catal.*, 2022, **12**, 3821.